To cite this version :

Hot dwell-fatigue behaviour of additively manufactured AlSi10Mg alloy: Relaxation, cyclic softening and fracture mechanisms

Jianguang Bao [a,b,*], Zhengkai Wu [c], Shengchuan Wu [c,*], Philip J. Withers [d], Fei Li [b,e], Saad Ahmed [d], Adil Benaarbia [f], Wei Sun [b]

[a] Research Institute of Aero-engine, Beihang University, Beijing 100191, China
[b] Faculty of Engineering, University of Nottingham, Nottingham NG7 2RD, United Kingdom
[c] State Key Laboratory of Traction Power, Southwest Jiaotong University, Chengdu 610031, China
[d] Henry Royce Institute, Department of Materials, University of Manchester, Manchester M13 9PL, United Kingdom
[e] Chengdu Aircraft Industrial (Group) CO., LTD, Chengdu, Sichuan 610092, China
[f] Arts et Métiers Institute of Technology, CNRS, Université de Lorraine, LEM3, F-57000 Metz, France

ABSTRACT

This paper presents the results of high temperature strain-range controlled low cycle fatigue tests of a laser powder bead fused AlSi10Mg alloy. Following stress relief (2hrs at 300 ℃), two cyclic loading waveforms (standard triangular and dwell-type trapezoidal waveforms) and three temperatures (100 ℃, 250 ℃ and 400 ℃) were applied to investigate both the mechanical response and the related microstructural changes of this additively manufactured (AM) aluminium alloy. The bulk mechanical responses were found to exhibit a continuous cyclic softening, decreasing stress relaxation and decreased energy dissipated per cycle. The stress relaxation is strongly affected by the test temperature rising to almost complete relaxation at 400 ℃. At lower temperatures (100 ℃ and 250 ℃), the higher the temperature the more subgrains are developed during cyclic loading. Up to 250 ℃, the subgrain size increases with temperature and laser powder bead fused defects preferentially act as the fatigue crack initiation sites. While at 400 ℃, coarse Si particles precipitate during cyclic deformation and a high density of microvoids are nucleated from these coarse Si precipitates, which grow and link up to cause failure, resulting in a dimple dominated ductile fracture.

1. Introduction

As an additive manufacturing (AM) technology, laser powder bead fusion (LPBF, originally termed selective laser melting) has spiked the interest of the automotive, medical, energy industries and especially aerospace fields due to the potential for cost reduction, fewer steps in the production process and increased design-freedom [1,2]. In this respect, AlSi10Mg alloys are attracting increasing interest in the aerospace industry owing to their suitability for AM (high fluidity, low shrinkage and good weldability), light weight and high corrosion resistance [3]. It has been reported that 55% of failures in aeronautic engineering and, more generally speaking, approximately 90% of all engineering failures are caused by a fatigue-related damage mechanisms [4,5]. Therefore, an in-depth physical understanding of the material degradation and fracture mechanisms of LPBF AlSi10Mg alloys under high temperature cyclic loading is needed to ensure their reliability, especially given the propensity for the LPBF process to generate a significant population of unwanted defects [6,7].

To date, low cycle fatigue (LCF) where plasticity plays an important role and elastic–plastic fracture mechanics is relevant, has been relatively unexplored for LPBF AlSi10Mg alloy materials [8], however much can be gleaned from the extensive work on the LCF performance of cast Al alloy. Tian et al. [9] found that during LCF of a cast A319 alloy, at higher strain amplitudes (0.35% − 0.4%), peak-aged samples exhibited continuous hardening while over-aged samples displayed continuous softening. Cai et al. [10,11] found that fatigue cracks tended to initiate from the shrinkage pores located at, or near, the specimen surface of cast AlSi10Mg(Cu) alloy, which is similar to the high cycle fatigue condition. Unsurprisingly, they found fatigue lives to be longer at 100 ℃ than that at 250 ℃ for all strain amplitudes with more dislocations activated at

higher temperature and dislocation climb around the strengthening precipitates becoming easier, leading to cyclic softening. Jeong [12] reported that cyclic softening of Al-Si-Mg alloy decreased with increasing Mn and Cu contents at 250 °C in the LCF regime. For a gravity cast Al-9Si-3Cu alloy, Fan et al. [13] observed cyclic hardening at 150 °C in contrast to cyclic softening at 250 °C. To date only Romano et al. [8] has studied the conventional LCF behaviour of the LPBF AlSi10Mg alloy, at room temperature proposing a model for elastic–plastic fatigue crack growth based on the known defect population inside the material, while elevated temperature studies are completely lacking.

A number of critical components experience not only elevated temperature cyclic loading conditions but also stable loading periods [14,15]. This raises the importance of the interaction between fatigue, creep and creep-fatigue in life assessment and design of these components. However, to date, very little work has been reported on the creep behaviour of AlSi10Mg alloy, especially with regards to the creep-fatigue interaction. In this respect it is important to note that additive manufacturing can lead to highly anisotropic microstructures and defect morphologies [16–18] leading to significant differences between the properties measured along the build direction and perpendicular to it [6,19].

The experimental work described here is aimed at investigating the cyclic behaviour of unnotched LPBF AlSi10Mg alloy, subjected to conventional fully reversed LCF and dwell-fatigue conditions in the temperature range 150–400 °C. It complements the elevated temperature in SEM crack propagation study conducted by Wang et al. [20] on single edge notched AlSi10Mg AM specimens who found that the effect of pre-existing pores were more important at low temperatures than at a temperature 400 °C and above. The overall mechanical responses are analysed first and the underlying physical mechanisms are discussed further in relation to the microstructure evolution over this temperature range.

2. Material and experimental programme

2.1. Material and LPBF process

The AlSi10Mg powder particles used for LPBF ranged from 15 − 45 μm in diameter (based on the sieving method). A 150 mm × 40 mm × 70 mm AlSi10Mg alloy wall structure was printed by using a BLT S310 LPBF machine (Xi'an Bright Laser Technologies Co., Ltd). The LPBF manufacturing parameters employed are summarised in Table. 1. A rotation of the scan direction between powder-bed layers of 67° was used, as shown in Fig. 1a, to minimise any in-plane (X-Y) anisotropy arising from the morphological and crystallographic texture. The build chamber was flooded with a protective atmosphere of Argon gas during the fabrication process, thereby ensuring an oxygen content < 100 ppm. No platform preheating was used for any of the builds. The chemical composition of the as-built structures was quantified by energy dispersive spectrometry (EDS) and is as follows (in wt. %): Al − 89.20; Si − 9.24; Mg − 0.32; O − 0.14; Fe − 0.68 plus trace element in accordance with the DIN EN 1706:2010 standard.

Subsequently, a thermal stress relief was performed at 300 °C for 2 h to relieve the residual stresses generated by the AM process as used elsewhere [21]. After the stress relief the specimens were machined from the as-built structure according to the specification given by the ISO 12,106 standard for axial strain controlled fatigue testing of metallic materials. In order to avoid the influence of build direction on material properties, all the samples were excised from the same block of material

Table 1
LPBF process parameters.

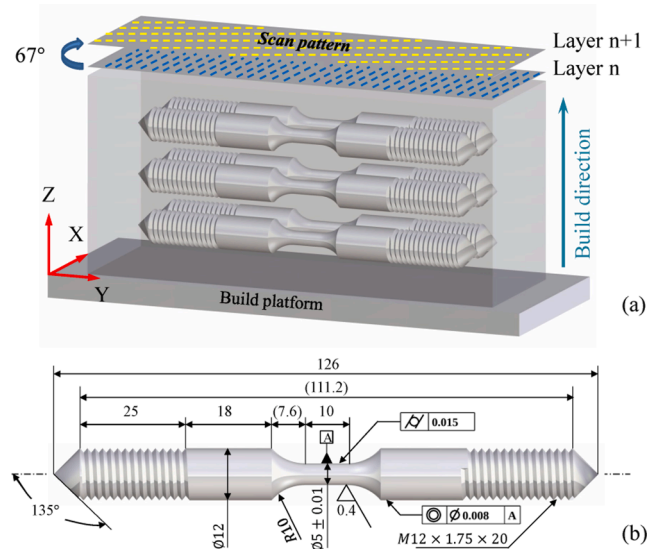| Laser power (W)	Layer thickness (mm)	Scanning speed (mm/s)	Scanline spacing (mm)
360–400	0.05	1200–1500	0.13–0.16

Fig. 1. Schematics showing (a) the extraction of test specimens from the as-received structure and (b) the dimensions (mm) of the fatigue test specimens. The platform material was 5A06 Al alloy and the LPBF build dimensions were 150 mm × 40 mm × 70 mm.

(Fig. 1a) with the loading axis perpendicular to the build direction (Z). The specimen geometry is shown in Fig. 1b. In view of the sensitivity of fatigue to the surface condition after machining, the specimens were ground and polished mechanically to avoid premature crack formation arising from surface roughness.

2.2. Fatigue testing

Standard LCF tests were carried out using a fully reversed standard triangular waveform (SWT) applied uniaxially under strain-controlled LCF testing (see Fig. 2a). In addition dwell-fatigue tests using a dwell-type trapezoidal waveform (DWT) were undertaken (see Fig. 2b). A constant strain rate of $0.02\%s^{-1}$, a strain amplitude of $\pm0.5\%$ and a loading ratio of $R = -1$ were applied in all tests. To investigate dwell-fatigue, a 150 min hold at peak tension during the first cycle and 5 min hold for every consecutive cycle were employed to ensure a quasi-equilibrium state of stress. These hold durations were determined to be sufficient to highlight and distinguish between fatigue and relaxation induced damage. To cover a range of operational temperatures appropriate to the AlSi10Mg alloy structures [20,22], three temperatures (i.e. 100 °C, 250 °C and 400 °C) were selected. The data was acquired continuously until specimen fracture. All experiments were carried out in air on Tinius Olsen H25KS electromechanical test rig controlled using Horizon software, see Fig. 2c. A proportional-integral-derivative (PID) controller mechanism was used to obtain the desired set points. A Mayes alignment fixture was used for angular and concentric adjustments needed to align the test arrangement. The test temperature was maintained via three K-type thermocouples attached to the three different zones of the samples. The displacement along the gauge length of the sample was measured using a pair of LVDT-0582 high temperature linear voltage differential side-contact transformer extensometers. The test rig was located in an air-conditioned room with an ambient temperature of approximately 20 °C. For more details of the experimental setup the reader is referred to the authors' previous work [23,24].

2.3. Microstructure characterisation

The as-stress relieved LPBF AlSi10Mg alloy microstructures were characterised by optical microscopy (OM), scanning electron microscopy (SEM) and transmission electron microscopy (TEM) after etching
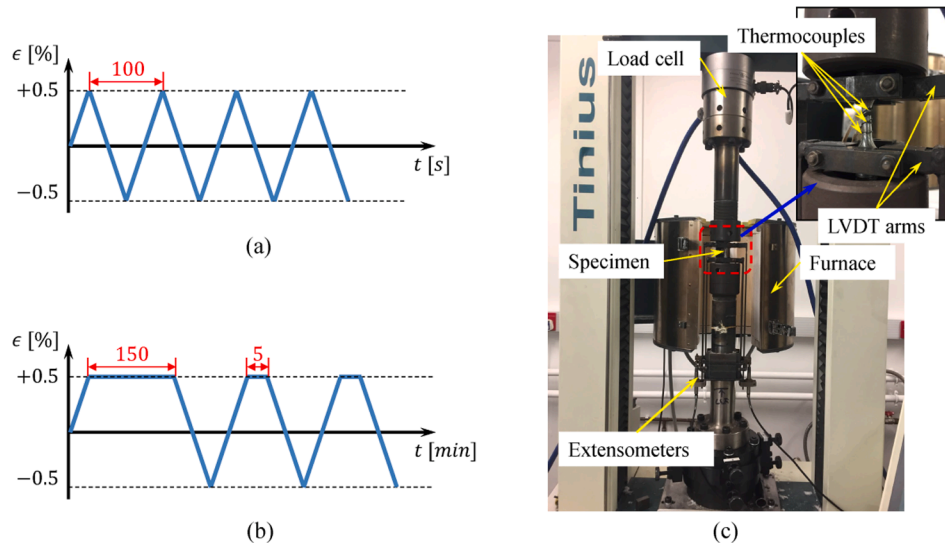
Fig. 2. Strain-time waveform employed for (a) conventional LCF testing using a saw-tooth profile (SWT) and (b) dwell-fatigue (DWT) loading alongside (c) the test set-up based on a Tinius Olsen H25KS electromechanical testing machine fitted with a DSCCTOL 25 kN pancake style load cell and a Severn Thermal Solutions SF2107 split section resistance furnace.

with Keller's reagent. Thin foils having the dimension of 3 mm × 3 mm × 20 μm were prepared by double-jet electropolishing using a nitric acid/methanol solution for TEM observation in a Tecnai G2 F30 S-TWIN with an accelerating voltage of 300 kV. After fractographic inspection, cross sectional samples were cut (parallel to the fatigue axis) from the fractured samples and polished following standard metallographic preparation process finished with a chemo-mechanical polishing process using a suspension of 0.06 μm colloidal silica. 2.5 h of Ar ion mill final polishing was then employed for high electron backscatter diffraction (EBSD) indexing rates. To obtain information regarding changes of the crystallographic orientation and size of grains, the microstructures of the as-manufactured and the fractured states were characterised by EBSD in a TESCAN MIRA-3 FEG SEM equipped with an Oxford Aztec C-Nano camera at an accelerating voltage of 20 kV with step sizes ranging from 0.1 μm − 2 μm. A 10° misorientation angle and a grain boundary completion angle down to 0° were used to define the grain boundaries. The EBSD data were processed using the HKL Channel 5 software from Oxford Instruments. Kernel average misorientation (KAM) was used to quantify the misorientation between the kernel point and its eight nearest neighbouring points [25]. To identify the phases and the morphologies, energy dispersive spectrometer (EDS) point scanning and X-ray mapping were conducted.

As-machined LPBF AlSi10Mg alloy test-pieces were computed tomography (CT) scanned at the Henry Moseley X-ray Imaging Facility (University of Manchester) using a Nikon Metrology 225/320 kV Custom Bay μCT machine to characterise the pores in 3D within the sample gauge volume prior to testing. Scanning was performed using a 80 kV accelerating voltage, a 62 μA current, an exposure time of 1000 ms and a molybdenum refection target. A voxel size of 11 μm was selected allowing the whole of the gauge volume of the fatigue specimens to be imaged. This is too coarse to resolve the finest defects, but is able to resolve and quantify defects 30 μm and larger which is sufficient to identify the critical defects.

To further investigate the defect characteristics, ruptured specimens were imaged by the high-resolution synchrotron radiation X-ray computed microtomography (SR-μCT) on beamline BL13W1 at the Shanghai Synchrotron Radiation Facility (SSRF) in Shanghai, China. Here a monochromatic 30 keV photon energy beam, which gives a voxel size of 3.25 μm, was used in combination with a 2048 × 2048 pixel CMOS detector located around 180 mm behind the sample. Each CT scan comprised 720 radiographs acquired over 180°, with an exposure time

of 1000 ms. Both before and after fatigue 3D Volumes were reconstructed from the 2D slices using the commercial software AVIZO®.

3. Results and analysis

3.1. Microstructure characterization of the as stress relieved material

The microstructure in the plane (X-Y) perpendicular to the build direction of the stress relieved material is illustrated in Fig. 3. As shown in Fig. 3a, it exhibits discontinuous melt paths ascribed to the laser penetration reflecting the 67° overlapping rotation angle between successive scans. In contrast to eutectic cellular microstructure representative of as-built LPBF AlSi10Mg alloy in reported previously [26] which shows an interconnected network of silicon decorating each cell, the morphology of solidification structure is less distinct, as shown in Fig. 3b arsing form the inter-diffusion of atoms during the stress relief treatment [27]. At higher magnification (Fig. 3c), it can be seen that the intercellular Si diffuses to form polygonal precipitates. The intergranular strengthening precipitates are too fine to see by SEM, but TEM (see Fig. 3d) shows that fine (~50 nm) Si precipitates form from the supersaturated α-Al matrix within the grain [28]. Similar microstructures have been reported previously for the stress relieved LPBF AlSi10Mg [21,27,29,30]. As shown in the inverse pole figure (IPF) map in Fig. 3e, the equiaxed grains are essentially randomly orientated. The fine grains are mainly located along the melt pool boundaries while the coarse ones lie in the melt pool core, which is ascribed to rapid solidification. Similar grain distributions have been observed by other researchers [17,31–33]. It can be seen from Fig. 3f that the grain size extends up to 40 μm although ~ 80% of the grain sizes lie in the 2–10 μm range.

The influence of the deposit layering orientation on porosity as well as the orientation of defects with respect to the cylinder longitudinal direction can be readily observed in the 3D renderings shown in Fig. 4a. Both irregular pancake shaped (lack of fusion) and spherical (gas porosity) defects are essentially randomly distributed. The former arise from incomplete melting during the LPBF process, while the latter arise from a combination of hydrogen evolution induced porosity and the remnant of shield gas [34,35]. It can be seen that the oblate 'pancake' shaped defects lie predominantly within the LPBF build plane as a result of the laser scan strategy which means they are oriented parallel to the specimen loading axis. Examples of spherical and oblate defects shown in Fig. 4a indicate the apparent difference in size and shape: the smaller
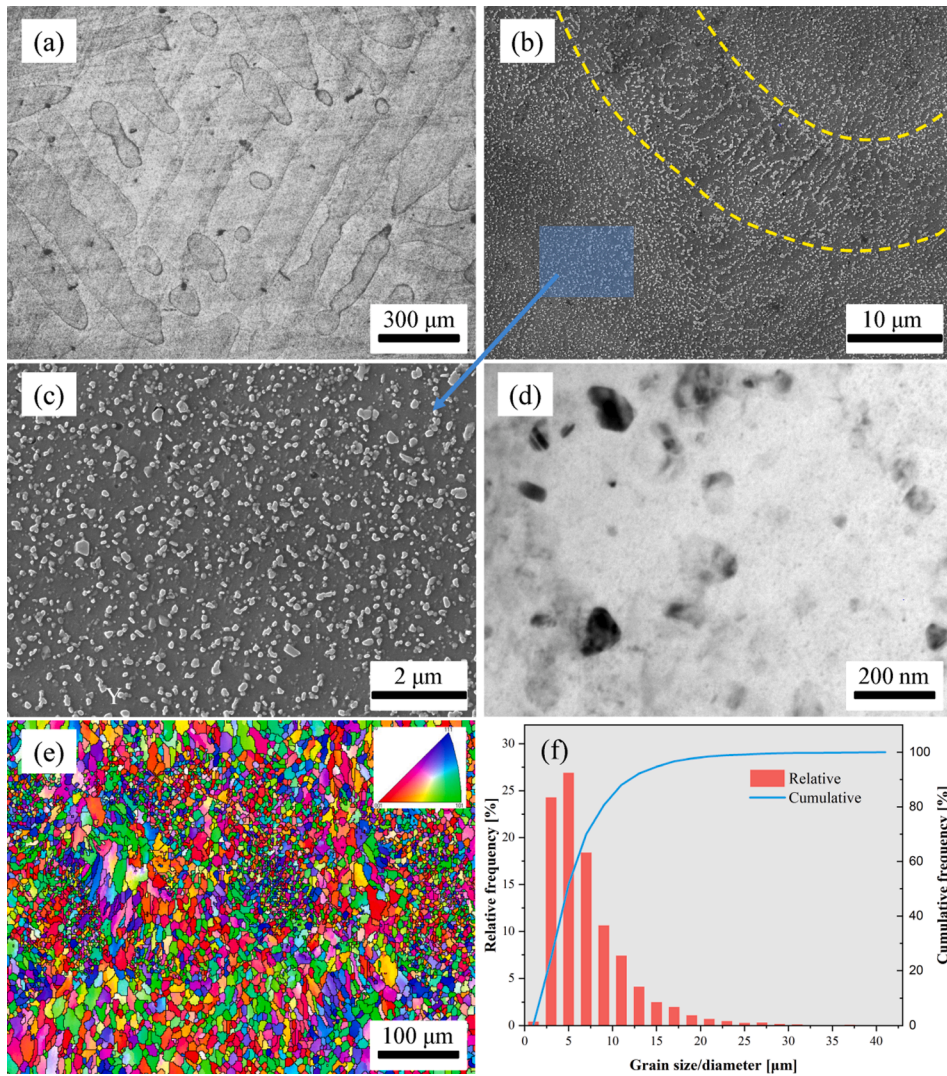
Fig. 3. (a) Optical micrograph, (b) low and (c) high magnification SEM microstructures, (d) TEM micrograph, (e) EBSD map and (f) grain size distribution of the LPBF AlSi10Mg alloy in the plane (X-Y) perpendicular to the build direction. The melt boundaries are shown by dashed lines.

the size the more spherical in shape. The scatter plot of the effective diameter and corresponding shapes of each defect, shown in Fig. 4c, confirms this observation. Fig. 4b reveals that approximately 90% of the defects are smaller than 100 μm.

3.2. Elevated temperature fatigue behaviour

In order to characterise the LCF behaviour of the LPBF AlSi10Mg alloy, hysteretic stress–strain responses at 100 °C, 250 °C and 400 °C are plotted in Fig. 5 (left). The main experimental findings are as follows: i) unsurprisingly the stress amplitudes decrease with increasing test temperature and the maximum stress decreases with increasing numbers of cycles highlighting the significance of cyclic softening; ii) the hysteresis loops become crescent shaped and shrink with a point tail in the compressive region in the later stages before rupture; iii) while the rate of change decreases, the area of the hysteresis loops never stabilizes with cycling before catastrophic failure; and iv) the fatigue lifetime is longer at 400 °C under the same strain amplitude, rate and ratio compared to the lower temperatures, which can also be gleaned from Fig. 9a. As shown in Fig. 5, temperature influences the mechanical response significantly under LCF and dwell-fatigue testing conditions: both the stiffness and stress amplitude decrease with increasing temperature.

The stress relaxation responses of under dwell-fatigue (DWT) are

shown in Fig. 5 (right). It is evident that apart from the response immediately on initiating the tensile unloading part of the cycle, the hysteresis loops are broadly similar to those reported for the SWT cycle, albeit with a slight reduction in the fatigue life, arising from the creep dwell. In addition to fatigue, creep damage is also accumulated during the hold periods. This observation is corroborated by the microstructure investigations conducted on fractured samples (discussed later). The stress relaxation responses during the initial long-dwell phase, the first and approximate 200th cycle (mid-life) are plotted in Fig. 6. It can be seen from Fig. 6a and b that the extent of stress relaxation during the long-dwell for the initial long hold is marked. As one would expect the stress relaxation is strongly dependent on the test temperature showing almost complete relaxation at 400 °C, while only ~ 23% and ~ 77% for 100 °C and 250 °C respectively. Around 50%, 70% and 80% of the decay has completed within the first 5 min at 100 °C, 250 °C and 400 °C respectively. The responses to the shorter subsequent dwell periods shown in Fig. 6c and d exhibit broadly similar behaviour with the peak stresses smaller for the mid-life when compared to the first cycle.

3.3. Microstructural evolution

The EBSD observations for the initial stress relieved structure, as well as the LCF and dwell-fatigued specimens are presented as IPF and KAM
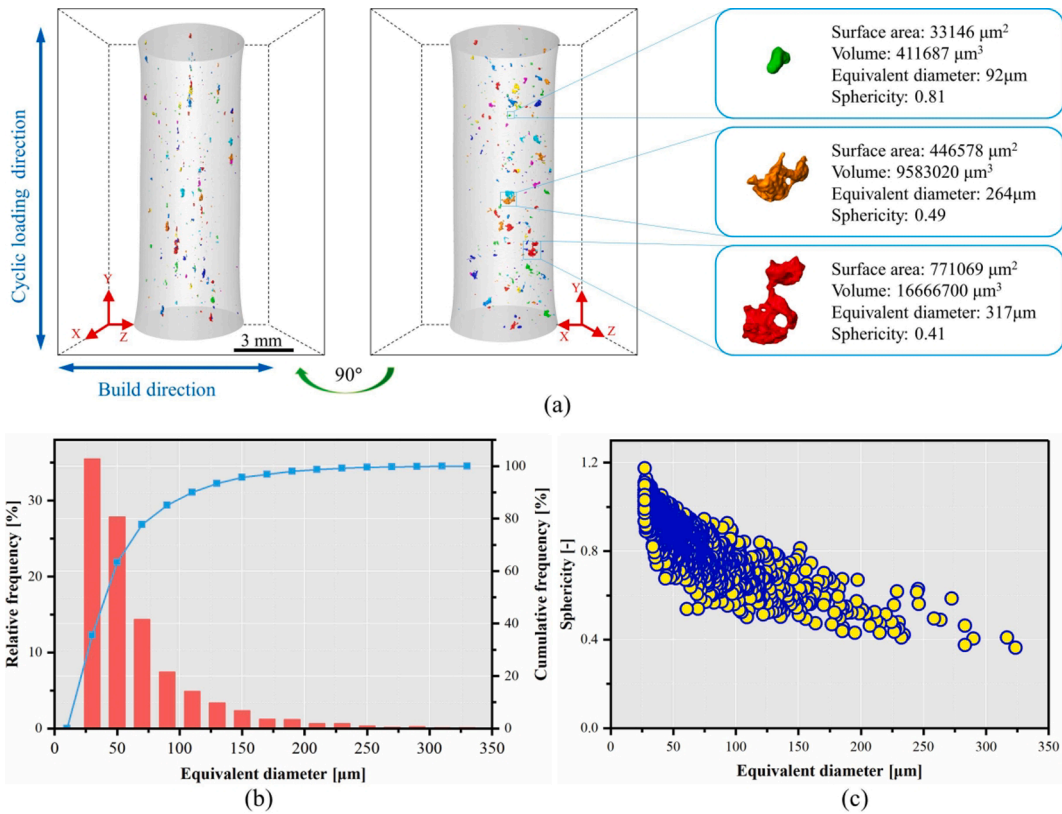
Fig. 4. (a) An X-ray CT 3D volume rendering of the micro-defects for the as-manufactured material viewed edge-on (LHS) and along (RHS) the build direction showing the preferred orientation of the larger pancake shaped defects. The false-colour coding is applied for clarity. (b) Distributions of equivalent diameter and its cumulative frequency curve and (c) distribution of defect sphericity with respect to the equivalent diameter (pore size).

maps in Fig. 7. It is apparent from the colour gradients within the grains that the samples fatigued at 100 °C exhibit significant misorientations, substructures and low-angle grain boundaries with even more extensive substructures at 250 °C [29]. It is also evident that grain coarsening becomes more extensive with increasing temperature as observed by others [29]. By contrast, more significant microstructural changes are evident after fatigue and dwell fatigue at 400 °C: i) the grain size is now significantly larger; ii) the grain shows little evidence of subgrains or grain misorientations; iii) microvoids are visible; and iv) a number of coarse Si particles are precipitated in common with previous work [36]. The KAM maps confirm the trends in the IPF maps, exhibiting an increasing tendency for intragrain misorientation at 100 °C and 250 °C. Furthermore, the misorientation is somewhat larger within grains than near original grain boundaries. By contrast the misorientations at 400 °C are comparable to the as-manufactured sample in both loading cases. Furthermore no regions of high misorientations are apparent in the vicinity of the voids.

With respect to the strengthening particles, it is clear that while the 100 °C and 250 °C fatigue treatments lead to little change in the Si distribution relative to the original 300 °C stress relieved state, the 400 °C exposure during fatigue on the other hand significantly coarsens the microstructure. Rather than the strengthening nanosized Si particles that have precipitated from the supersaturated α-Al solid solution in the stress relieved condition, at 400 °C significant coursing has occurred, as shown in Fig. 8 . This is consistent with the aforementioned EBSD measurements with the Si particles preferentially dispersed along the grain boundaries. As has been reported previously, the Si particle size has a significant effect on strengthening [36], such that the material at 400 °C would be expected to be significantly softened enhancing the ductility. These large particles can also act as preferential void nucleation sites (see section 3.4). In addition the Mg maps suggest some intergranular Si and Mg_2Si precipitates.

3.4. Fractography and final failure

As shown in Fig. 9, topography of the fracture surfaces was examined by SE imaging to investigate the fracture modes. It can be seen from Fig. 9a that for the samples tested at 100 °C and 250 °C the fracture surface comprises a fatigue crack initiation (FCI) zone, a fatigue crack propagation zone and a fast fracture zone. As highlighted by the yellow dashed ellipses, the FCI sites originate from internal LPBF defects lying close to the surface. Further, river-like tearing ridges and secondary cracks are evident in the low and high magnification fractographs, implying a quasi-cleavage fracture mode of the LPBF AlSi10Mg alloy under these temperature conditions [37]. By contrast for fatigue at 400 °C, the fracture surfaces display a dimpled surface with no apparent FCI site, which implies increased ductile fracture characteristics. It is noteworthy that no conspicuous differences are detected between the fracture surfaces for fatigue and dwell-fatigue samples at the same temperatures. This suggests that the creep dwell does not significantly affect the fatigue fracture mode [38].

As presented in Fig. 9a, both internal and near surface defects act as initiation sites under LCF of the LPBF AlSi10Mg in common with observations on materials [39]. While some fatigue studies have been undertaken on cast Al-Si alloys [40–42] and on additively manufactured AlSi10Mg [6–8,27], relatively little work have been reported for LCF on bulk specimen under elevated temperature conditions [10]. In terms of the fracture mechanism, in common with previous room temperature tests [8], it is apparent from Fig. 9 that at 100 °C and 250 °C, the LPBF AlSi10Mg structures preferentially fracture via fatigue cracks initiated from the LPBF defects. As shown in Fig. 10 2D slices and 3D re-constructions of fractured specimens obtained by SR-μCT demonstrate a significant difference in microvoid population between samples fatigued at 100 °C and 250 °C and those at of 400 °C which show 10 times more voids. Further cross sectional SEM examinations to 400 °C fatigued
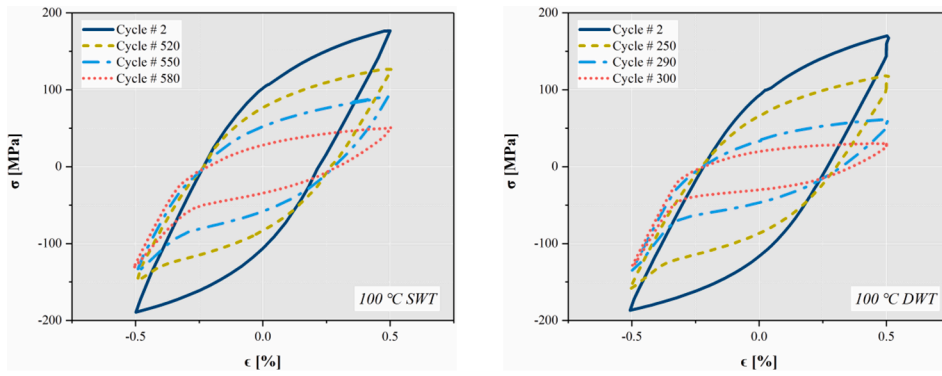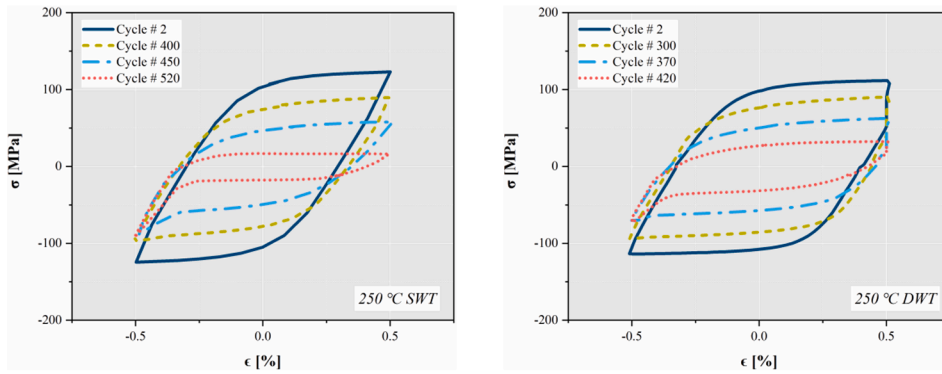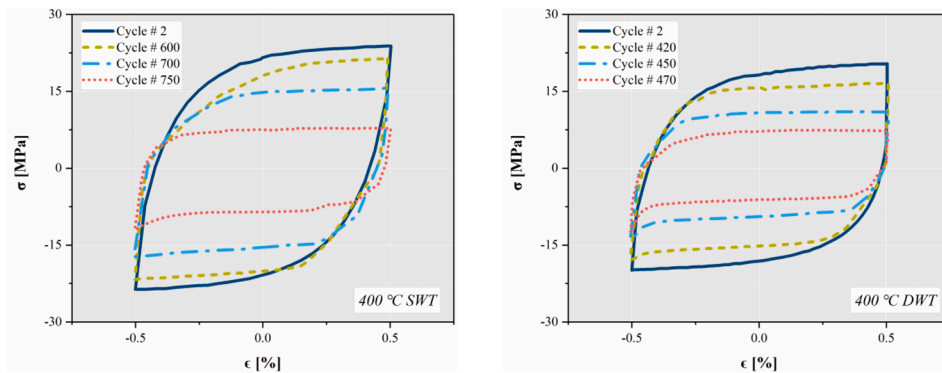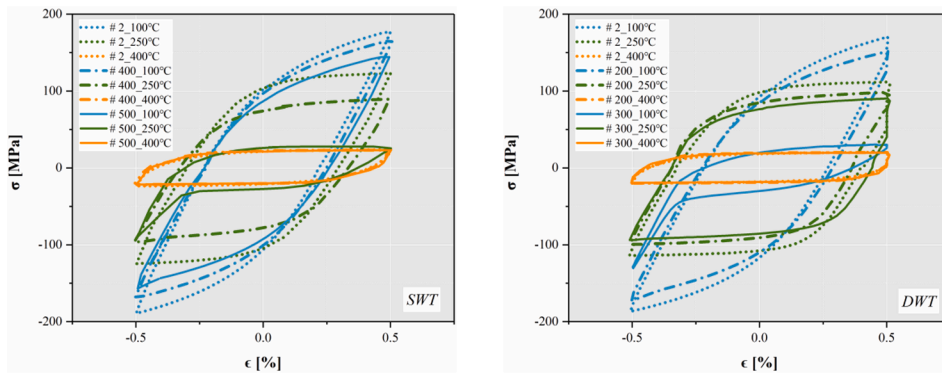
Fig. 5. Stress–strain curves with increasing number of cycles extracted for the standard triangular waveform (SWT) representative of LCF tests (left) and the dwell-fatigue (DWT) tests (right) conducted at temperatures of (a) 100 ℃, (b) 250 ℃ and (c) 400 ℃ respectively. Please note the significant difference between the Y-axis scales for the 400 ℃ graphs compared to those for 100 ℃ and 250 ℃. Hysteresis loops for typical cycles at the different tests temperatures are compared in (d).
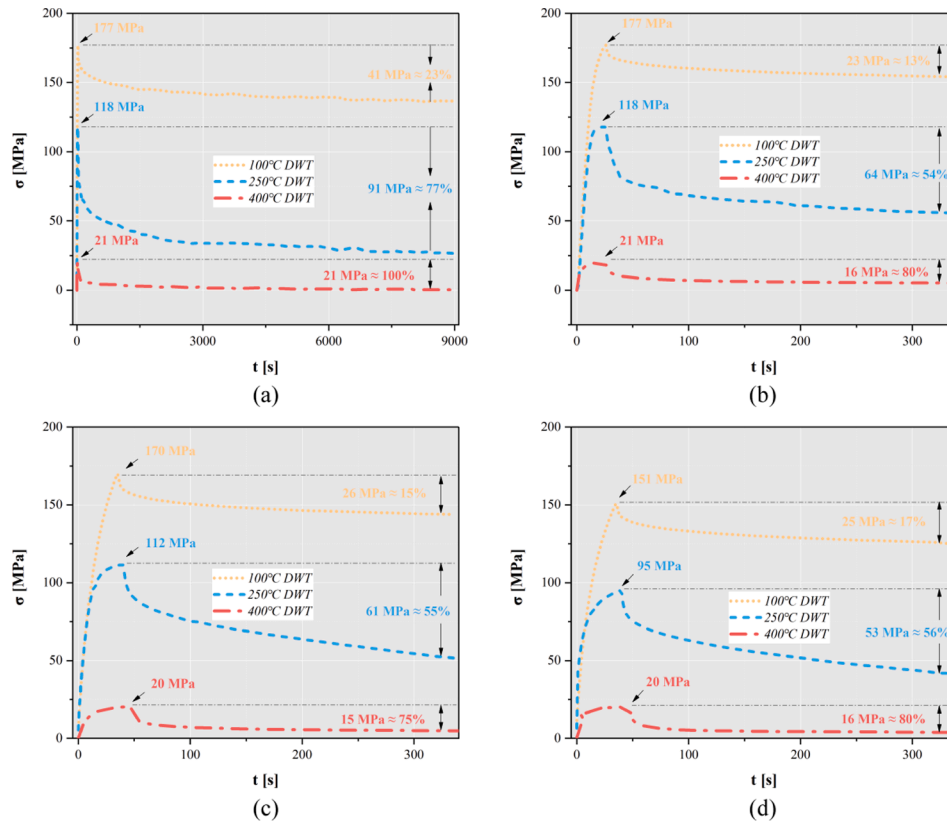
Fig. 6. The stress versus time response during the hold stage highlighting the relaxation behaviour of the LPBF AlSi10Mg alloy during (a) the entire and (b) the initial 5 min long dwell phase, (c) 1st short dwell cycle and (d) after ~ the 200th cycle (~mid-life).

specimen shown in Fig. 11 reveals that these additional microvoids nucleate from Si precipitates, which is mainly ascribed to the decohesion of Si precipitates from Al-matrix in common with Ref [26]. This is induced by the plastic incompatibility between the plastically hard Si precipitates and the ductile Al-matrix during the cyclic plasticity. Given the ductile dimples and the absence of large LOF defects on the fracture surface (Fig. 9a-iii) it would seem reasonable to conclude that the growth and coalescence of these high density microvoids dominates the fracture mechanism during fatigue at 400 ℃.

4. Discussion

4.1. Cyclic softening behaviour

The evolution of stress range, $\Delta\sigma/2$, and hysteresis area, A_h, with the number of cycles are shown in Fig. 12 for fatigue cycles with and without the dwell. At 100 ℃, a continuous cyclic softening response can be seen in Fig. 12a under both LCF and dwell-fatigue cycling. In common with observations of elevated temperature LCF on other systems, three different stages can be distinguished in the stress amplitude curve: i) the first stage shows a relatively rapid non-linear decrease in both the tensile and compressive peak stresses due to an increase in inelastic strain per cycle, ii) a period when the softening per cycle is small, and iii) the final stage showing a sharp decrease in the stress amplitude leading to failure. With increasing temperature, stage I becomes less distinct such that by 400 ℃ it is essentially absent. Fig. 12b shows that the energy dissipation each cycle varies largely in line with the changes in stress amplitude. At all temperatures the three degradation stages occur after fewer cycles for dwell fatigue than for LCF.

Insights into the underlying mechanisms that govern this behaviour may be gained from the statistical analysis of the KAM maps shown in Fig. 13. It can be seen that the frequency of local misorientation ranging

between $0.5° − 3°$ is somewhat higher for the dwell-fatigued samples than in the LCF samples at the same temperatures, indicating that more subgrains are developed by introducing the dwells [10]. The extensive formation of subgrains arises from the greater rearrangement of dislocations at elevated temperatures [38] resulting in a decrease in dislocation density and contributing to the cyclic softening. Moreover, changes in the morphology of the Si from a dense population of micron sized intergranular Si and nanoscale intragranular Si particles to a much coarser distribution of intergranular Si particles leads to the significant decrease in the strength by Orowan strengthening and dislocation pileup [43].

It is clear that the softening arises from a decreasing density of obstacles to dislocation motion and an increasing tendency for dislocation to be able to climb past these obstacles with rising temperature. This is corroborated by Fig. 13, which shows that the frequency of local misorientations in the range of $0.5° − 3°$gradually increase with temperature from room temperature to 250 ℃, which implies the higher temperature the more dislocation activated and promotes the dislocation climbing, which further contribute to cyclic softening [10,44].

4.2. Fracture mechanisms at elevated temperatures

As illustrated schematically in Fig. 14, the LCF fatigue fracture mechanisms of LPBF AlSi10Mg alloy change as the temperature is increased. At 100 ℃ and 250 ℃, both the internal and near surface LPBF defects act as stress/strain concentrators during LCF from which fatigue cracks nucleate and subsequently propagate by the repeated plastic blunting-sharpening process leading to fatigue fracture [11]. Additionally, this LPBF defect induced fatigue fracture mode generally results in significant scatter in LCF life due to the stohchastic nature of the size, shape and location of the defects [16,35,45]. However, at 400 ℃, the extensive plasticity means that there is less of a tendency for the LPBF
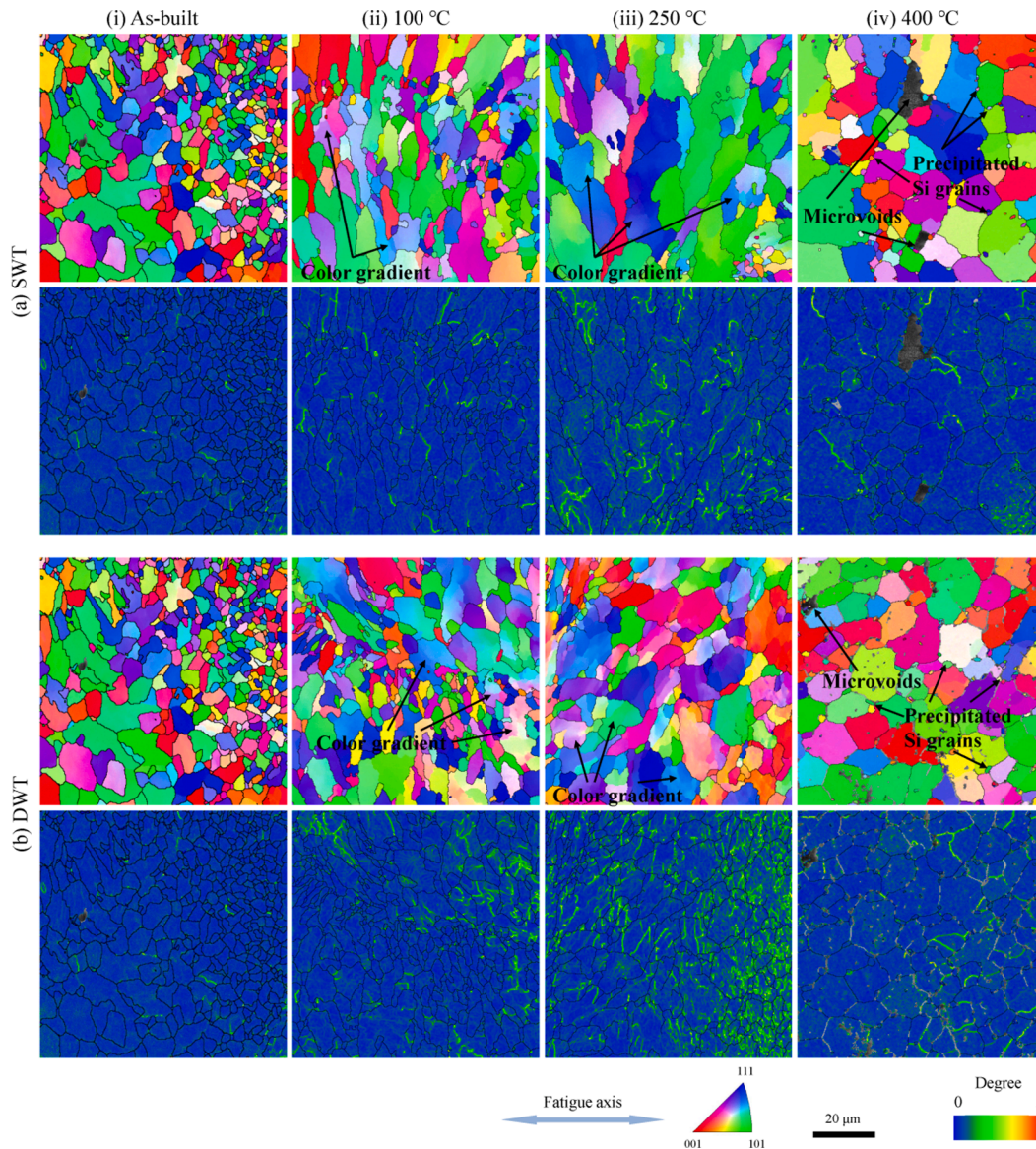
Fig. 7. Comparison of EBSD results between the as-built (with stress relieved) material and samples fatigued to failure for a) fatigued and dwell fatigue testes samples with the IPF maps (top) and KAM maps (bottom) where blue corresponds to low misorientation level, and red indicates the high misorientation levels. For the failed samples the areas studied were located within ~ 100 μm of the fracture surface.

defects to act as critical defects; rather the large number of microvoids occurring at the large Si particles developed by the 400 °C exposure become significant. The growth and coalescence of this high density microvoid gradually fail the material during cyclic deformations and eventually leave the dimple like micromorphology on the fatigue fracture surface. It is noteworthy that although the fracture mode of this alloy at 400 °C is clear, given the propensity of large defects in AM materials, the competition mechanism between initial defects and microvoids occurred from Si precipitates, during LCF needs to be quantified further. Indeed, the LPBF defects may play a bigger role when tested parallel to the build direction because they present a much larger projected area in the crack plane in this orientation [6].

5. Conclusions

This study characterises the effects of temperature, creep dwell and LPBF defects on microstructure change during LCF, which in turn results in different behaviours as a function of temperature. The following conclusions can be drawn:

i. The stress relief treatment at 300 °C breaks up the eutectic Si network decorating the grains somewhat and enables the intragranular precipitation of nanoscale Si particles from the supersaturated Al matrix leading to a high strength microstructure prior to fatigue testing.

ii. The stress relieved LPBF AlSi10Mg alloy exhibits a continuous cyclic softening, decelerated stress relaxation and decreased energy dissipated per cycle at elevated temperatures.

iii. The fatigue behaviour for conventional LCF and dwell fatigue are broadly the same although the various stress relaxation stages occur after fewer cycles for the latter.

iv. The stress relaxation is strongly affected by the test temperature rising to almost complete relaxation at 400 °C.

v. At lower temperatures (100 °C and 250 °C) subgrains are developed during cyclic loading the more so at 250 °C.

vi. At 400 °C, the microstructure evolves significantly coursing the intergranular Si particles and the fine intragranular particles leading to significant softening and increased dislocation climb.
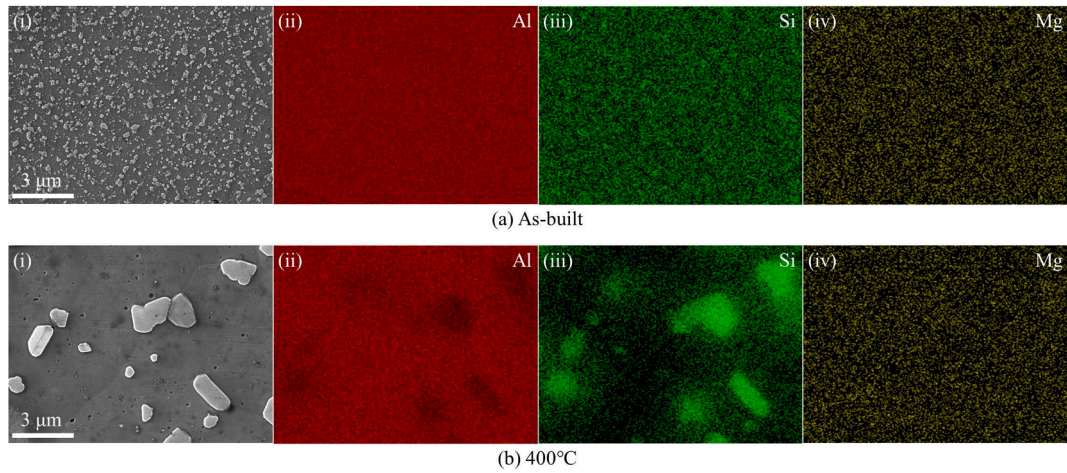
Fig. 8. Representative SEM images and EDS maps for (a) stress relieved material and (b) after fatigue at 400 ℃ sample showing the microstructural change that occurs during SWT at 400℃.
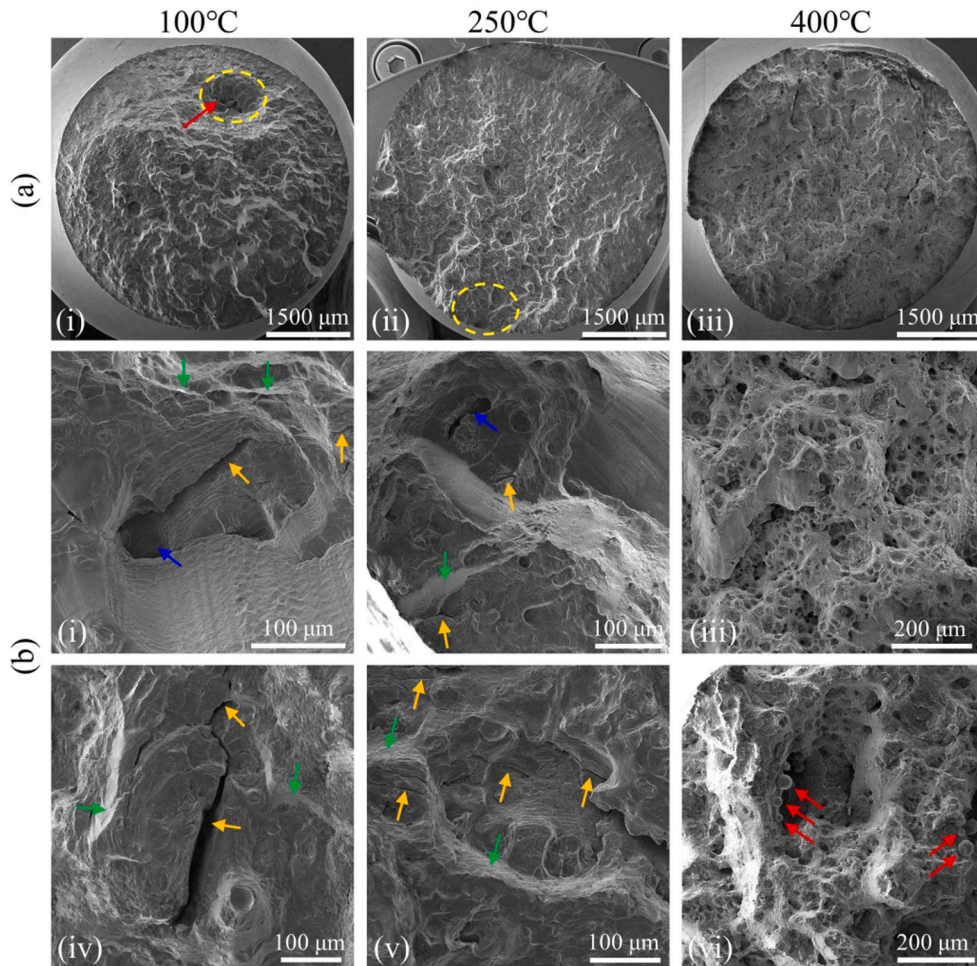

Fig. 9. Fractographs at (a) low and (b) high magnifications showing the facture surfaces for 100 ℃, 250 ℃ and 400 ℃ fatigued specimens. (i)-(iii) correspond to SWT and (iv)-(vi) to DWT specimens. Yellow dashed ellipses highlight the FCI sites, red arrows unmelted powder, blue arrows the pores, green the tearing ridges and orange arrows the secondary cracks.

vii. LPBF defects act as preferential the crack initiation sites during the LCF failure process at 100 ℃ and 250 ℃ conditions and finally lead to quasi-cleavage fatigue fracture. However at 400 ℃, a high density microvoids are nucleated from the coarse Si particles. During cyclic deformation these grow and coalesce giving rise to ductile dimple dominated fatigue fracture.
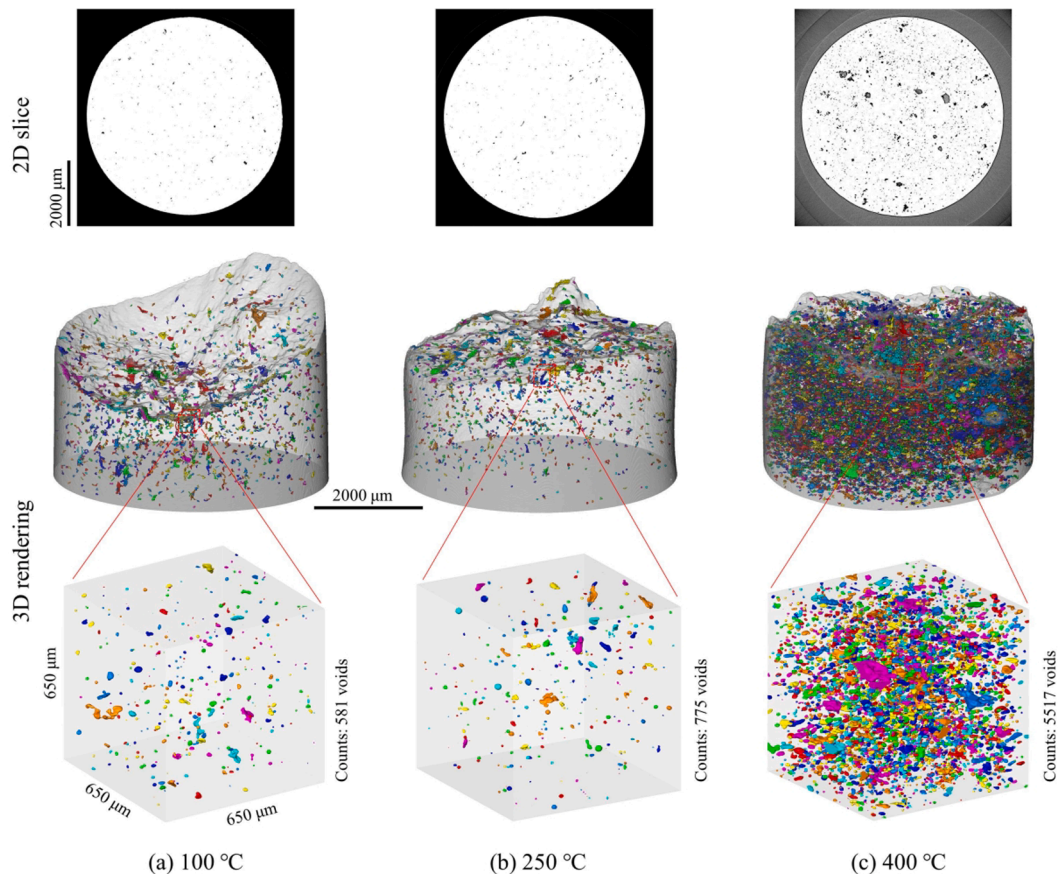
Fig. 10. 3D volume renderings of SR-µCT scans of ruptured specimens showing the distinct populations of microvoids between for samples tested at (a) 100 ℃, (b) 250 ℃ and (c) the 400 ℃. The false-colour coding is applied for clarity.
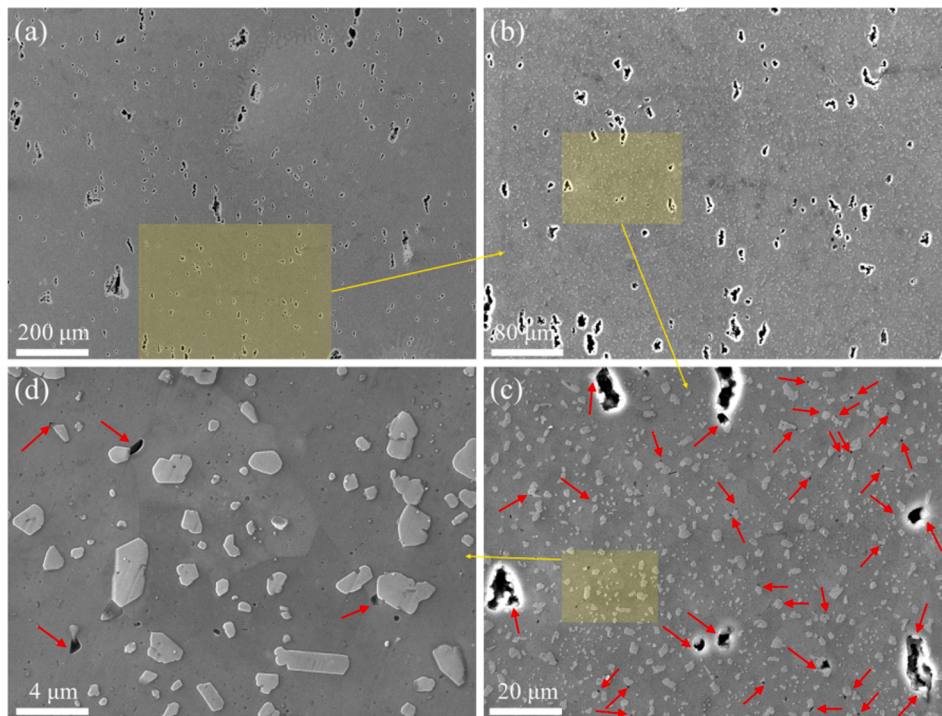

Fig. 11. Cross-sectional SEM images taken from a 400 ℃ SWT fatigued specimen with increasing magnification a) d) showing microvoids nucleating from Si precipitates, which are highlighted by red arrows. The imaged zones are located within ~ 2 mm away from the fracture surface.
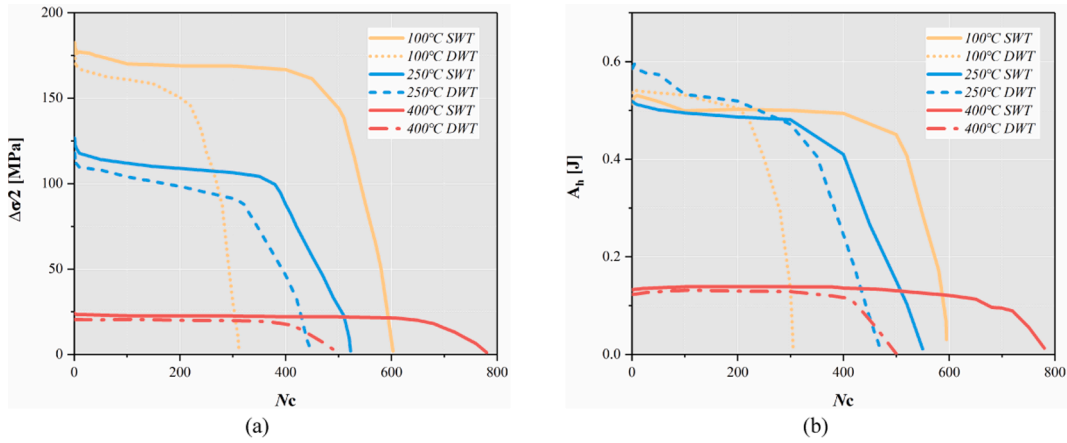
Fig. 12. Comparison plots showing the variation in (a) the stress amplitude and (b) energy dissipated per hysteresis cycle for both LCF (solid lines) and dwell-fatigue (dashed lines).
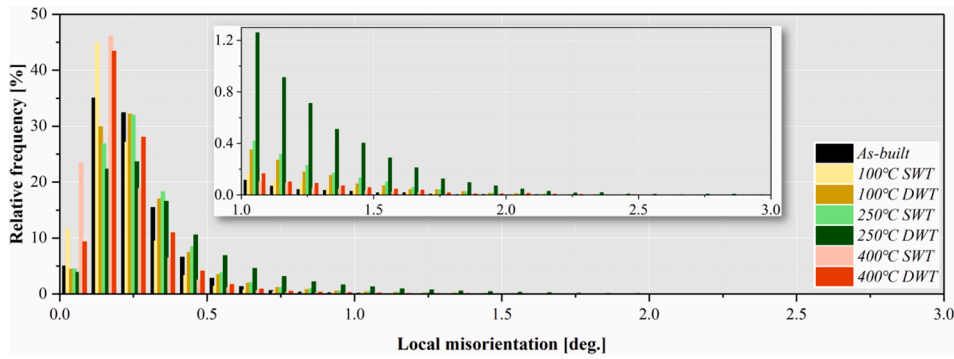

Fig. 13. Statistical analysis of the relative frequency of local misorientation as a function of angle from 0° to 3° derived from the KAM maps in Fig. 7.
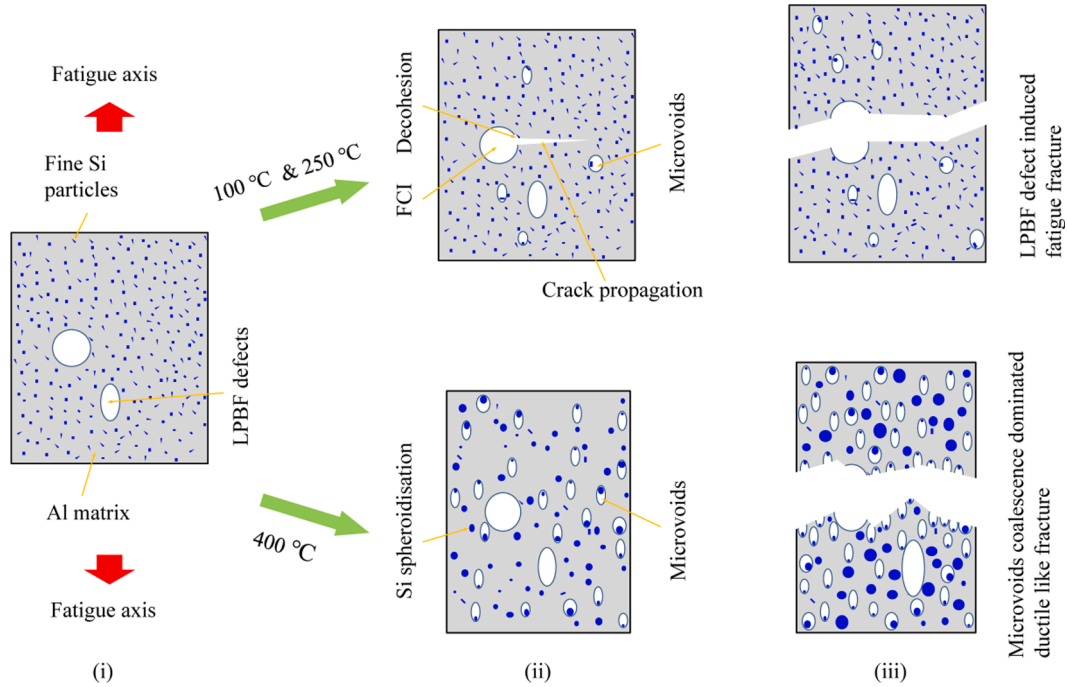

Fig. 14. Schematic representations of LCF fracture mechanisms of the LPBF AlSi10Mg alloy at high temperature conditions (100 ℃, 250 ℃ and 400 ℃). Surface defects induced fracture mode at 100 ℃ and 250 ℃ is not illustrated here due to the similar process as internal defect mode.

Declaration of Competing Interest

The authors declare that they have no known competing financial interests or personal relationships that could have appeared to influence the work reported in this paper.

References

[1] Martin JH, Yahata BD, Hundley JM, Mayer JA, Schaedler TA, Pollock TM. 3D printing of high-strength aluminium alloys. Nature 2017;549:365–9. https://doi.org/10.1038/nature23894.

[2] Yap C, Chua C, Dong Z, Liu Z, Zhang D, Loh L, et al. Review of selective laser melting: Materials and applications. Appl Phys Rev 2015;2. https://doi.org/10.1063/1.4935926.

[3] Tang M, Pistorius PC. Oxides, porosity and fatigue performance of AlSi10Mg parts produced by selective laser melting. Int J Fatigue 2017;94:192–201. https://doi.org/10.1016/j.ijfatigue.2016.06.002.

[4] Uzan NE, Shneck R, Yeheskel O, Frage N. Fatigue of AlSi10Mg specimens fabricated by additive manufacturing selective laser melting (AM-SLM). Mater Sci Eng A. 2017;704:229–37. https://doi.org/10.1016/j.msea.2017.08.027.

[5] Campbell GS, Lahey R. A survey of serious aircraft accidents involving fatigue fracture. Int J Fatigue 1984;6:25–30. https://doi.org/10.1016/0142-1123(84)90005-7.

[6] Larrosa NO, Wang W, Read N, Loretto MH, Evans C, Carr J, et al. Linking microstructure and processing defects to mechanical properties of selectively laser melted AlSi10Mg alloy. Theor Appl Fract Mech 2018;98:123–33. https://doi.org/10.1016/j.tafmec.2018.09.011.

[7] Bao J, Wu S, Withers P, Wu Z, Li F, Fu Y, et al. Defect evolution during high temperature tension-tension fatigue of SLM AlSi10Mg alloy by synchrotron tomography. Mater Sci Eng A. 2020;792. https://doi.org/10.1016/j.msea.2020.139809.

[8] Romano S, Patriarca L, Foletti S, Beretta S. LCF behaviour and a comprehensive life prediction model for AlSi10Mg obtained by SLM. Int J Fatigue. 2018. https://doi.org/10.1016/j.ijfatigue.2018.07.030.

[9] Tian D, Liu X, He G, Shen Y, Lv S, Wang Q. Low cycle fatigue behavior of casting A319 alloy under two different aging conditions. Mater Sci Eng A. 2016;654:60–8. https://doi.org/10.1016/j.msea.2015.12.023.

[10] Cai C, Geng H, Cui Q, Wang S, Zhang Z. Low cycle fatigue behavior of AlSi10Mg (Cu) alloy at high temperature. Mater Charact 2018;145:594–605. https://doi.org/10.1016/j.matchar.2018.09.023.

[11] Cai C, Geng H, Zhang Z. Temperature-dependent cyclic response and microstructure of AlSi10Mg(Cu) alloy. Mater Charact 2018. https://doi.org/10.1016/j.matchar.2018.04.042.

[12] Jeong CY. High temperature mechanical properties of AlSiMg(Cu) alloys for automotive cylinder heads. Mater Trans 2013. https://doi.org/10.2320/matertrans.M2012285.

[13] Fan K, Liu X, He G, Chen H. Elevated temperature low cycle fatigue of a gravity casting Al-Si-Cu alloy used for engine cylinder heads. Mater Sci Eng A. 2015. https://doi.org/10.1016/j.msea.2015.02.069.

[14] Evans WJ, Jones JP, Williams S. The interactions between fatigue, creep and environmental damage in Ti 6246 and Udimet 720Li. Int J Fatigue 2005. https://doi.org/10.1016/j.ijfatigue.2005.06.029.

[15] J. Kumar, A.K. Singh, S. Ganesh Sundara Raman, V. Kumar, Creep-fatigue damage modeling in Ti-6Al-4V alloy: A mechanistic approach, Int. J. Fatigue. 98 (2017). 10.1016/j.ijfatigue.2017.01.016.

[16] Xu Z, Wang Q, Wang X, Tan C, Guo M, Gao P. High cycle fatigue performance of AlSi10mg alloy produced by selective laser melting. Mech Mater 2020;148. https://doi.org/10.1016/j.mechmat.2020.103499.

[17] Thijs L, Kempen K, Kruth JP, Van Humbeeck J. Fine-structured aluminium products with controllable texture by selective laser melting of pre-alloyed AlSi10Mg powder. Acta Mater 2013;61:1809–19. https://doi.org/10.1016/j.actamat.2012.11.052.

[18] Xu Z, Liu A, Wang X. The influence of building direction on the fatigue crack propagation behavior of Ti6Al4V alloy produced by selective laser melting. Mater Sci Eng A. 2019;767. https://doi.org/10.1016/j.msea.2019.138409.

[19] Wu Z, Wu S, Bao J, Qian W, Karabal S, Sun W, et al. The effect of defect population on anisotropic fatigue resistance of selective laser melted AlSi10Mg alloy. Int J Fatigue 2021. https://doi.org/10.1016/j.ijfatigue.2021.106317.

[20] Wang Z, Wu W, Qian G, Sun L, Li X, Correia JAFO. In-situ SEM investigation on fatigue behaviors of additive manufactured Al-Si10-Mg alloy at elevated temperature. Eng Fract Mech 2019;214:149–63. https://doi.org/10.1016/j.engfracmech.2019.03.040.

[21] Fiocchi J, Tuissi A, Bassani P, Biffi CA. Low temperature annealing dedicated to AlSi10Mg selective laser melting products. J. Alloys Compd 2017;695. https://doi.org/10.1016/j.jallcom.2016.12.019.

[22] Uzan NE, Shneck R, Yeheskel O, Frage N. High-temperature mechanical properties of AlSi10Mg specimens fabricated by additive manufacturing using selective laser melting technologies (AM-SLM). Addit Manuf 2018;24:257–63. https://doi.org/10.1016/j.addma.2018.09.033.

[23] Rae Y, Benaarbia A, Hughes J, Sun W. Experimental characterisation and computational modelling of cyclic viscoplastic behaviour of turbine steel. Int J Fatigue. 2019;124:581–94. https://doi.org/10.1016/j.ijfatigue.2019.01.022.

[24] Rae Y, Guo X, Benaarbia A, Neate N, Sun W. On the microstructural evolution in 12% Cr turbine steel during low cycle fatigue at elevated temperature. Mater Sci Eng A. 2020;773. https://doi.org/10.1016/j.msea.2019.138864.

[25] Rui S, Shang Y, Su Y, Qiu W, Niu L, Shi H, et al. EBSD analysis of cyclic load effect on final misorientation distribution of post-mortem low alloy steel: A new method for fatigue crack tip driving force prediction. Int J Fatigue 2018. https://doi.org/10.1016/j.ijfatigue.2018.04.016.

[26] Delahaye J, Tchuindjang JT, Lecomte-Beckers J, Rigo O, Habraken AM, Mertens A. Influence of Si precipitates on fracture mechanisms of AlSi10Mg parts processed by Selective Laser Melting. Acta Mater 2019. https://doi.org/10.1016/j.actamat.2019.06.013.

[27] Zhang C, Zhu H, Liao H, Cheng Y, Hu Z, Zeng X. Effect of heat treatments on fatigue property of selective laser melting AlSi10Mg. Int J Fatigue 2018. https://doi.org/10.1016/j.ijfatigue.2018.07.016.

[28] Zhao L, Santos Macías JG, Ding L, Idrissi H, Simar A. Damage mechanisms in selective laser melted AlSi10Mg under as built and different post-treatment conditions. Mater Sci Eng A. 2019;764:138210. https://doi.org/10.1016/j.msea.2019.138210.

[29] Takata N, Kodaira H, Sekizawa K, Suzuki A, Kobashi M. Change in microstructure of selectively laser melted AlSi10Mg alloy with heat treatments. Mater Sci Eng A. 2017;704:218–28. https://doi.org/10.1016/j.msea.2017.08.029.

[30] Fousová M, Dvorský D, Michalcová A, Vojtěch D. Changes in the microstructure and mechanical properties of additively manufactured AlSi10Mg alloy after exposure to elevated temperatures. Mater Charact 2018;137:119–26.

[31] Tiwari JK, Mandal A, Sathish N, Agrawal AK, Srivastava AK. Investigation of porosity, microstructure and mechanical properties of additively manufactured graphene reinforced AlSi10Mg composite. Addi Manuf 2020. https://doi.org/10.1016/j.addma.2020.101095.

[32] Amir B, Samuha S, Sadot O. Influence of selective laser melting machine source on the dynamic properties of AlSi10Mg Alloy. Mater. (Basel). 2019;12. https://doi.org/10.3390/ma12071143.

[33] Paul MJ, Liu Q, Best JP, Li X, Kruzic JJ, Ramamurty U, et al. Fracture resistance of AlSi10Mg fabricated by laser powder bed fusion. Acta Mater 2021. https://doi.org/10.1016/j.actamat.2021.116869.

[34] Romano S, Abel A, Gumpinger J, Brandão AD, Beretta S. Quality control of AlSi10Mg produced by SLM: Metallography versus CT scans for critical defect size assessment. Addit Manuf 2019;28:394–405. https://doi.org/10.1016/j.addma.2019.05.017.

[35] Hu Y, Wu S, Withers PJ, Zhang J, Bao H, Fu Y, et al. The effect of manufacturing defects on the fatigue life of selective laser melted Ti-6Al-4V structures. Mater Des 2020. https://doi.org/10.1016/j.matdes.2020.108708.

[36] W. Li, S. Li, J. Liu, A. Zhang, Y. Zhou, Q. Wei, C. Yan, Y. Shi, Effect of heat treatment on AlSi10Mg alloy fabricated by selective laser melting: Microstructure evolution, mechanical properties and fracture mechanism, Mater. Sci. Eng. A. 663 (n.d.) 116–125. 10.1016/j.msea.2016.03.088.

[37] Wang M, Pang J, Qiu Y, Liu H, Li S, Zhang Z. Tensile Strength Evolution and Damage Mechanisms of Al–Si Piston Alloy at Different Temperatures. Adv Eng Mater 2018;20:1–9. https://doi.org/10.1002/adem.201700610.

[38] Benaarbia A, Xu X, Sun W, Becker AA, Osgerby S. Characterization of cyclic behavior, deformation mechanisms, and microstructural evolution of MarBN steels under high temperature conditions. Int J Fatigue. 2020. https://doi.org/10.1016/j.ijfatigue.2019.105270.

[39] Tammas-Williams S, Withers PJ, Todd I, Prangnell PB. The Influence of Porosity on Fatigue Crack Initiation in Additively Manufactured Titanium Components. Sci Rep 2017;7:1–13. https://doi.org/10.1038/s41598-017-06504-5.

[40] Nicoletto G, Konečná R, Fintova S. Characterization of microshrinkage casting defects of Al-Si alloys by X-ray computed tomography and metallography. Int J Fatigue. 2012;41:39–46. https://doi.org/10.1016/j.ijfatigue.2012.01.006.

[41] Dezecot S, Maurel V, Buffiere JY, Szmytka F, Koster A. 3D characterization and modeling of low cycle fatigue damage mechanisms at high temperature in a cast aluminum alloy. Acta Mater 2017;123:24–34. https://doi.org/10.1016/j.actamat.2016.10.028.

[42] Serrano-Munoz I, Buffiere JY, Mokso R, Verdu C, Nadot Y. Location, location & size: Defects close to surfaces dominate fatigue crack initiation. Sci Rep 2017;7:1–9. https://doi.org/10.1038/srep45239.

[43] Alghamdi F, Song X, Hadadzadeh A, Shalchi-Amirkhiz B, Mohammadi M, Haghshenas M. Post heat treatment of additive manufactured AlSi10Mg: On silicon

morphology, texture and small-scale properties. Mater Sci Eng A. 2020;783. https://doi.org/10.1016/j.msea.2020.139296.

[44] Kamaya M. Measurement of local plastic strain distribution of stainless steel by electron backscatter diffraction. Mater Charact 2009;60:125–32. https://doi.org/10.1016/j.matchar.2008.07.010.

[45] Xu Z, Liu A, Wang X. Fatigue performance and crack propagation behavior of selective laser melted AlSi10Mg in 0°, 15°, 45° and 90° building directions. Mater Sci Eng A. 2021;812. https://doi.org/10.1016/j.msea.2021.141141.